Contractility, focal adhesion orientation, and stress fiber orientation drive cancer cell polarity and migration along wavy ECM substrates

Robert S. Fischer[a], Xiaoyu Sun[b,1], Michelle A. Baird[a], Matt J. Hourwitz[b], Bo Ri Seo[c,2], Ana M. Pasapera[a], Shalin B. Mehta[d], Wolfgang Losert[e,f], Claudia Fischbach[c], John T. Fourkas[b,f], and Clare M. Waterman[a,3]

[a]Cell and Developmental Biology Center, National Heart Lung and Blood Institute, NIH, Bethesda, MD 20892; [b]Department of Chemistry and Biochemistry, University of Maryland, College Park, MD 20742; [c]Meinig School of Biomedical Engineering, Cornell University, Ithaca, NY 14850; [d]Microscopy Platform, CZ Biohub, San Francisco, CA 94158; [e]Department of Physics, University of Maryland, College Park, MD 20742; and [f]Institute for Physical Science and Technology, University of Maryland, College Park, MD 20742

This contribution is part of the special series of Inaugural Articles by members of the National Academy of Sciences elected in 2018.

Contributed by Clare M. Waterman, March 5, 2021 (sent for review October 9, 2020; reviewed by Christopher S. Chen, Alexander R. Dunn, and Manuel Thery)

Contact guidance is a powerful topographical cue that induces persistent directional cell migration. Healthy tissue stroma is characterized by a meshwork of wavy extracellular matrix (ECM) fiber bundles, whereas metastasis-prone stroma exhibit less wavy, more linear fibers. The latter topography correlates with poor prognosis, whereas more wavy bundles correlate with benign tumors. We designed nanotopographic ECM-coated substrates that mimic collagen fibril waveforms seen in tumors and healthy tissues to determine how these nanotopographies may regulate cancer cell polarization and migration machineries. Cell polarization and directional migration were inhibited by fibril-like wave substrates above a threshold amplitude. Although polarity signals and actin nucleation factors were required for polarization and migration on low-amplitude wave substrates, they did not localize to cell leading edges. Instead, these factors localized to wave peaks, creating multiple "cryptic leading edges" within cells. On high-amplitude wave substrates, retrograde flow from large cryptic leading edges depolarized stress fibers and focal adhesions and inhibited cell migration. On low-amplitude wave substrates, actomyosin contractility overrode the small cryptic leading edges and drove stress fiber and focal adhesion orientation along the wave axis to mediate directional migration. Cancer cells of different intrinsic contractility depolarized at different wave amplitudes, and cell polarization response to wavy substrates could be tuned by manipulating contractility. We propose that ECM fibril waveforms with sufficiently high amplitude around tumors may serve as "cell polarization barriers," decreasing directional migration of tumor cells, which could be overcome by up-regulation of tumor cell contractility.

polarization | tumor ECM | topography | cancer | contractility

One hallmark of tumor progression to more advanced stages and worsening patient prognosis is the remodeling of the extracellular matrix (ECM) in the tumor microenvironment by fibroblasts (1) and macrophages (2). In several tumor types—including breast (3, 4), skin (5), ovary (6, 7), colon (2), and liver (8)—such remodeling is characterized by stiffening and reorganization of normally wavy stromal collagen bundles into thick linear bundles. Linear bundles are thought to provide "tracks" to mediate metastatic cell migration out of the primary tumor, whereas curved or wavy bundles typical of normal stroma are thought to inhibit cell movement (9, 10). The notion that linear ECM fibers support tumor metastasis arose from the long-standing observation that cells of many types polarize and migrate directionally in response to anisotropic physical cues, such as linear fibrils or grooves in a substrate, in a process called contact guidance (11). In support of this, ovarian cancer cells migrate more actively on ECM substrates that mimic the collagen architecture of aggressive ovarian tumors than on those mimicking normal or benign stroma (12). It is thought that the effects of comorbidities on ECM architecture, for example obesity in which breast stroma exhibits more linear collagen bundles than seen in lean tissue, may predispose patients to worse clinical outcomes when cancer does arise (13). However, a direct link between metastasis and the migratory behavior of cancer cells in response to linear or wavy or ECM fibril architecture has not been established, and the mechanisms by which such regulation might occur are unknown.

Cell polarization and migration in response to anisotropic cues during contact guidance, chemotaxis, haptotaxis, or durotaxis is mediated by similar molecular mechanisms. Polarization is initiated by ligand binding by growth factor or ECM receptors that promote Rho GTPases (14, 15), and is enforced by spatial

Significance

Tumor progression to enable metastasis includes remodeling the wavy bundles of collagen making up the tissue stromal extracellular matrix (ECM) into straight bundles within the tumor microenvironment. While wavy collagen bundles are thought to be inhibitory to cell polarization and migration in tissue, straight ECM fibers are thought to be conducive, thereby mediating metastasis. We used nanofabricated cell culture substrates that mimic the ECM fiber waveforms seen in both benign- and metastases-promoting tumor ECMs. Large amplitude ECM waves depolarized tumor cells and decreased directional migration via cell contractility-mediated organization of the cytoskeleton and adhesions. Thus, ECM architecture of normal tissue and benign tumors may generally inhibit tumor cell exit, but this may be overcome by increasing tumor cell contractility.

Author contributions: R.S.F. and X.S. designed research; R.S.F., M.A.B., B.R.S., A.M.P., and C.F. performed research; X.S., M.J.H., S.B.M., W.L., and J.T.F. contributed new reagents/analytic tools; R.S.F. analyzed data; and R.S.F., C.F., J.T.F., and C.M.W. wrote the paper.

Reviewers: C.S.C., Boston University; A.R.D., Stanford University; and M.T., Commissariat à l'Energie Atomique.

The authors declare no competing interest.

[1]Present address: Structural Mechanics and Mechanobiology, The Rockefeller University, New York, NY 10065.

[2]Present address: School of Engineering and Applied Sciences, Harvard University, Cambridge, MA 02138.

[3]To whom correspondence may be addressed. Email: watermancm@nhlbi.nih.gov.

This article contains supporting information online at https://www.pnas.org/lookup/suppl/doi:10.1073/pnas.2021135118/-/DCSupplemental.

Published May 24, 2021.

segregation of phosphatidylinositol 3-kinase (PI3K) at the leading edge to produce phosphatidylinositol-3,4,5-triphosphate (PIP3) and the phosphatase and tensin homolog (PTEN) removing PIP3 at the cell rear (16–18). PIP3 and Rho GTPases at the leading edge promote polarization of the microtubule cytoskeleton and Golgi apparatus, as well as actin polymerization via Arp2/3 and formins (19–23), to drive leading-edge protrusions. Retrograde flow of the polymerizing actin network at the leading edge is coupled to integrin-based focal adhesions (FAs) via a molecular clutch (24, 25), which engages FAs to the ECM. Recruitment of myosin II to the polymerizing actin contracts the network, creating actin arcs and stress fibers in the lamella, maturing the FAs and orienting them in the direction of cell migration (26–30). Disassembly of FAs toward the rear of the cell allows forward movement (31–35). Artificial enforcement of this organization of actin polymerization and adhesions by micropatterned ECMs alone is sufficient to define the polarity of the cell, independent of other stimuli (36). However, how these molecular mechanisms are modulated by the differing stromal collagen architectures associated with normal or tumor tissue is not known.

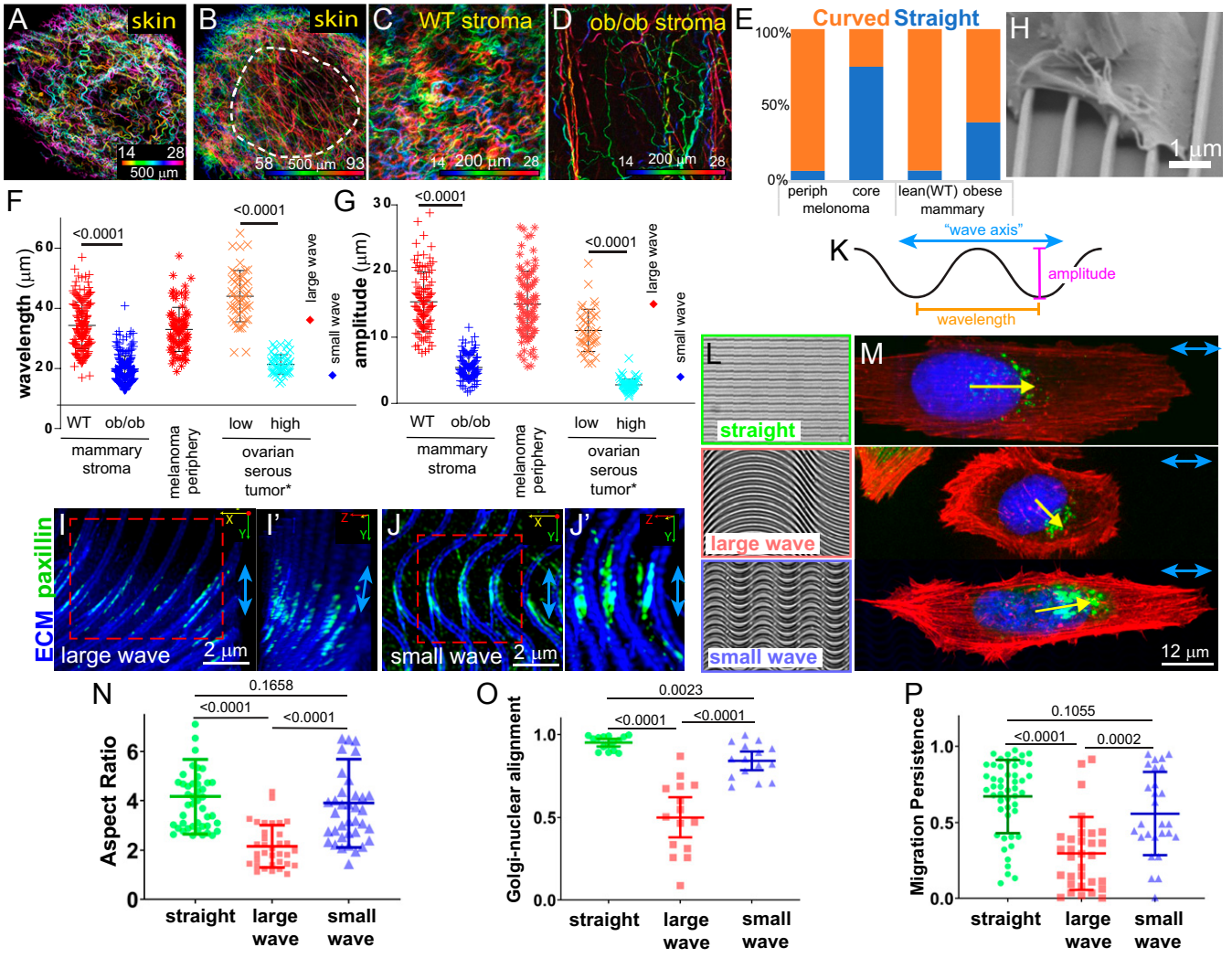

Fig. 1. Fibril-like ECM wave amplitude regulates cancer cell polarization and migration. SHG microscopy (*A–D*) and image analysis (*E–G*) of collagen fibers in mouse tumor models and tissues. (*A–D*) Maximum-intensity *z*-projections of confocal image stacks (color scale = *z*-depth) [Scale bars, 500 μm (*A* and *B*) or 200 μm (*C* and *D*)]. (*A* and *B*) Region of tumor formed from 1205Lu human melanoma cells in nude [Crl:NU(NCr)-Foxn1^{nu}] mice at the (*A*) outer 14 μm and (*B*) central 35 μm of image planes through the tumor; dashed line (*B*), boundary between periphery and core. (*C* and *D*) Mammary fat pad ECM in *C* wild-type C57BL/6 (WT, "lean") and (*D*) ob^{-}/ob^{-} mouse. (*E*) Percentage of curved ($1/r > 0.03$ μm, orange) and straight ($1/r < 0.03$ μm, blue) collagen-fiber segments. $n = 2{,}196$, 2,197, 1,184, and 1,905 point curvatures from melanoma periphery, core, lean, and obese adipose tissues, respectively. (*F* and *G*) Wavelength and amplitude of wave-like segments of collagen fibers in melanoma tumors or mammary fat pad as in *A–D*, as well as from mages published in Alkmin et al. (12) of human ovarian serous tumors with low or high metastatic potential. Large-wave and small-wave points indicate the wavelength and amplitude of ECM fibril wave substrates used in *I–P*; $n = 90$, 168, 227, 64, 51, and 51 segments from melanoma periphery, melanoma core, lean and obese mammary, high- and low-grade serous ovarian tissues, respectively. (*H*) SEM image of U2OS cell on a wave substrate. (*I* and *J*) Maximum-intensity *z*-projections STED image stacks of paxillin (green) and fibronectin (blue) in U2OS cells adhered to fibronectin-coated small- and large-wave wave substrates. (*I′* and *J′*) Zoomed, ~75° rotation of regions in *I* and *J*. (*K*) Diagram of ECM wave properties. (*L*) Phase-contrast images of (*Top*) straight, (*Middle*) large-wave, and (*Bottom*) small-wave ECM fibril substrates. (*M*) Maximum-intensity *z*-projections of confocal stacks of U2OS cells plated on adjacent substrates in *L* and stained for F-actin (phalloidin, red), Golgi (GM130, green), and nucleus (DAPI, blue). Yellow arrows: axis between centers-of-mass of Golgi and nuclear fluorescence. (*N–P*) Cell polarization measured in U2OS cells by aspect ratio (*N*), Golgi-nucleus axis alignment relative to wave axis (*O*), or migration persistence from time-lapse movies of HEY T30 cells (*P*), plotted as a function of waveform. $n = 46$, 34, and 38 U2OS (*N* and *O*) cells or 49, 32, and 27 HEY T30 cells (*P*) on straight, small-wave and large-wave substrates. Blue arrows: wave axis. Long bars = mean; short bars = SD. Pairwise Mann–Whitney tests are shown.

Here we sought to examine the contact-guidance–mediated polarization and migration responses of tumor cells to ECM fibril architectures mimicking those seen in normal and tumor stroma, and to dissect the mechanisms of these responses. We designed synthetic nanotopographic ECM-coated substrates that approximate collagen fibril size and the range of waveforms observed in tumors and tissues from mouse and human samples, and we determined their effect on the organization and dynamics of the cell polarity and migration machineries. We find that cell polarization and directional migration are inhibited by sinusoidal fibril-like waves above a threshold amplitude by geometrically constrained effects on the organization of actomyosin contractility and FA orientation. Importantly, we found that cancer cells of different intrinsic contractility depolarized at different ECM-wave amplitudes, and that cell polarization could be tuned on wavy substrates by manipulating contractility. Thus, the ECM-fibril waveform, in addition to other factors in the tumor microenvironment, may regulate cancer cells' ability to migrate out of

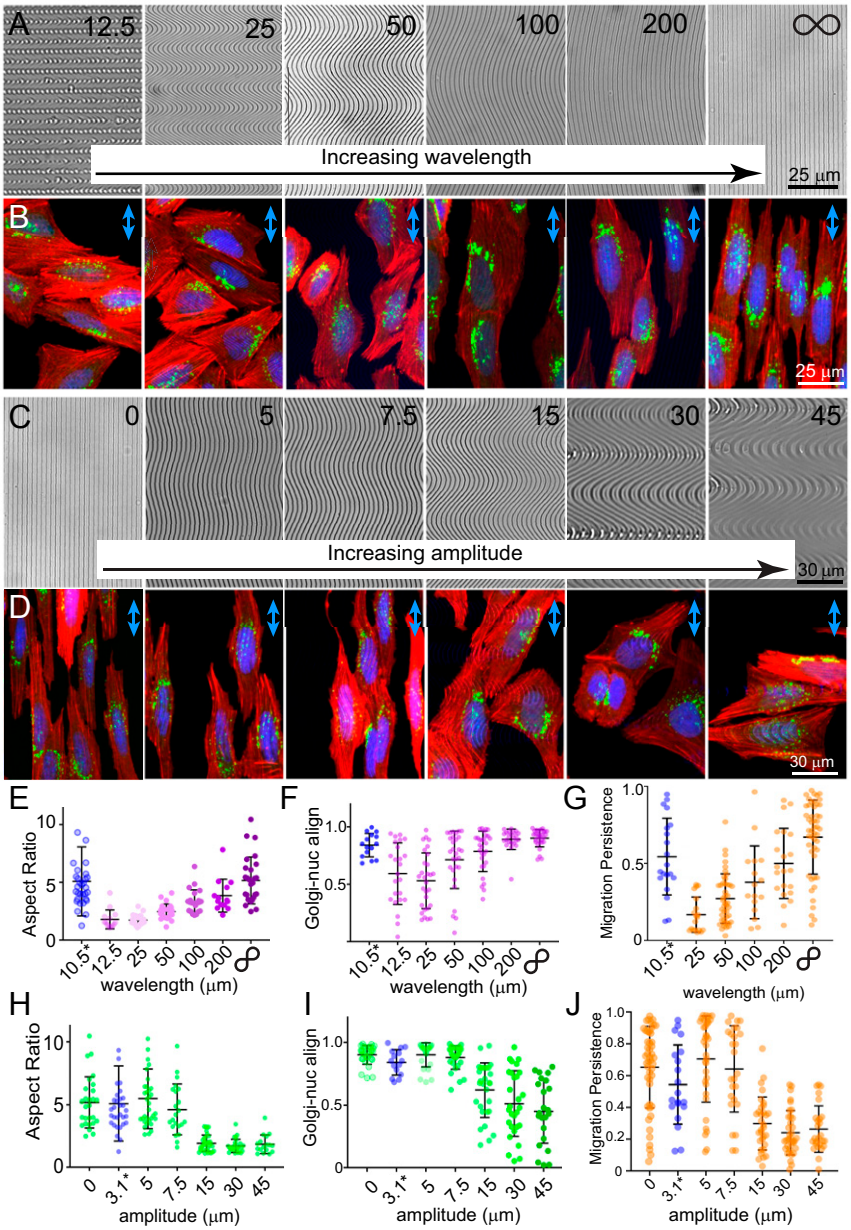

Fig. 2. ECM waves promote cell polarization and migration below a threshold of wave amplitude. (*A–F*, *H*, and *I*) Imaging and analysis of U2OS cells adhered to collagen-coated wave substrates. Phase-contrast images of substrates with (*A*) waves of constant amplitude (15 μm) and increasing wavelength and (*C*) constant wavelength (50 μm) and increasing amplitude. (*B* and *D*) Maximum-intensity *z*-projections of confocal stacks of cells on substrates above in *A* and *C* stained for F-actin (phalloidin, red), Golgi (GM130, green), and nucleus (DAPI, blue). Cell polarization measured in U2OS cells by aspect ratio (*E* and *H*), Golgi-nucleus axis alignment relative to wave axis (*F* and *I*), or migration persistence (*G* and *J*) from time-lapse movies of HEY T30 cells, plotted as a function of wavelength (*G*) and wave amplitude (*J*). (*E* and *F*) $n = 14$, 20, 21, 14, and 27 cells for 12.5, 25, 50, 100, 200, and straight, respectively. (*H* and *I*) $n = 29$,15, 25, 29, 29, 29, and 23 cells for straight, 5, 7.5, 15, 30, and 45, respectively. (*G*) $n = 16$, 19, 44, 16, 21, and 49 cells for 12.5, 25, 50, 100, 200, and straight, respectively. (*J*) $n = 48$, 35, 26, 32, 35 and 26 cells for straight, 5, 7.5, 15, 30, and 45, respectively. Datapoints in blue (*) are from cells plated on small-wave substrates (as defined in Fig. 1 *F* and *G*; data in Fig. 1 *N–P*) for comparison; note that wavelength and amplitude are both decreased relative to series. Blue arrows: wave axis. Long bars = mean; short bars = SD. Pairwise Mann–Whitney *t* tests are given in *SI Appendix*, Table S1.

tumors, and their contractility level may dictate the range of ECM architectures that allow migration.

Results

Fibril-like ECM Wave Amplitude Regulates Cancer Cell Polarization and Migration. To characterize the polarization and migratory responses of cancer cells to ECM fibril waveform, we first measured the approximate curvature, wavelength, and amplitude of ECM fibrils in the tumor microenvironment and tissues in mouse models. Tumors were generated by intradermal injection of metastatic 1205Lu human melanoma cells (37) into nude [Crl:NU(NCr)-Foxn1^{nu}] mice. We also examined mammary fat pads in either lean wild-type or obese ob/ob mice (B6.Cg-Lep^{ob}/J). Collagen fibrils imaged by intravital second harmonic-generation (SHG) microscopy (Fig. 1 *A* and *B* and Movies S1 and S2) exhibited a range of architectures, from relatively straight to curvy, often having a roughly repeating periodicity approximating wave-like forms. Curvature measurements of collagen fibril segments in skin tumors showed that the fraction of nearly straight fibrils ($1/r < 0.03$ μm) decreased from the tumor core, where most fibrils were relatively straight, to the tumor periphery, where most fibrils were curved (Fig. 1 *B* and *E* and *SI Appendix*, Fig. S1*A*). In mammary fat pads, most fibrils were curved in lean mice, whereas most were straight in obese mice (13) (Fig. 1 *C–E* and *SI Appendix*, Fig. S1*A*). Measurement of the approximate wavelength and amplitude of collagen fibril wave-like forms in our images and in previously published images of human ovarian tumors (7) showed that wavelength and amplitude were lower in mammary fat pads of ob/ob mice and high-grade ovarian tumors compared to those in fat pads of wild-type mice and low-grade ovarian tumors (Fig. 1 *F*, *G*, and *K*). Thus, collagen fibrils exhibit a wavy architecture that varies as a function of location within the tumor microenvironment, obesity-associated fibrosis, or tumor grade, such that tumor cores, obese tissue, and high-grade tumors contain ECM fibrils with low amplitudes and short wavelengths.

We next generated coverslip substrates with rows of aligned, fibronectin-coated, fibril-sized (600-nm high, 300-nm wide, 3-μm spacing) stiff linear acrylic ridges with waveforms that mimic those measured for ECM fibers in tumors of lower and higher metastatic potential (Fig. 1 *K* and *L*) (38). Although the spacing and stiffness of the substrate ridges was not fully physiological, the ridges provided fibril-like dimensions and full control of waveform parameters. Scanning-electron and stimulated emission depletion (STED) microscopies of U2OS osteosarcoma cells adhered to these substrates showed that cells appeared to "grab" the three-dimensional (3D) ridges, adhering via paxillin-containing FA to all the ridge surfaces, approximating the interaction of a cell with a collagen fibril in 3D (Fig. 1 *H–J* and Movies S3 and S4). "Large-wave" (15-μm amplitude, 50-μm wavelength) fibril-like substrates were similar to ECM bundles in the periphery of skin tumors, low serous ovarian tumors, and lean fat pad, while "small-wave" (3.1-μm amplitude, 10.5-μm wavelength) fibril-like substrates mimicked skin and high serous tumor and obese fat pad ECM fibrils. Cells were stained for actin, Golgi, and DNA markers and polarization responses to straight, large-wave, or small-wave substrates were quantified by two metrics: Cell elongation was defined as the ratio of the long-to-short axes of an ellipse fit to the cell area; cell polarization was the angle of a line defined by the centers of mass of DNA and Golgi fluorescence distributions relative to the peak-to-peak axis of fibril-like waves (the "wave axis" in Fig. 1 *K* and *O*). This showed that cells were similarly extended and polarized on straight and small-wave substrates, but exhibited significantly reduced elongation and polarization on large-wave substrates (Fig. 1 *N* and *O*). Analysis of movies of HEY-T30 ovarian tumor cells (that migrate more robustly that U2OS cells) showed that they underwent directionally persistent migration on straight and small-wave substrates, and reduced persistence on large-wave substrates (Fig. 1*P* and Movie S5). This shows that cancer cells polarize and migrate on low-amplitude, low-wavelength fibril-like substrates that mimic ECMs in more aggressive tumor microenvironments, while their migration is inhibited on large amplitude and wavelength substrates that mimic normal stroma ECMs.

We next performed a systematic examination of the effects of ECM architecture on cell morphology and behavior. To determine which aspects of large-wave fibril-like substrates promoted cell depolarization, we generated two series of wave substrates: one with the large-wave amplitude constant (15 μm) and wavelength varied from 12 to 200 μm (Fig. 2*A*); and one with the large-wave wavelength constant (50 μm) and amplitude varied from 5 to 45 μm (Fig. 2*C*). Analysis showed that for a fixed 15-μm amplitude, U2OS cell elongation and polarization and HEY-T30 migration persistence all increased directly with substrate wavelength, suggesting that polarized motility is inhibited by short wavelength (Fig. 2 *E–G* and Movie S6). However, the small-wave substrates described above that mimicked ECM fibers found in aggressive tumors promoted polarization and directed migration despite their short wavelength, suggesting that low amplitude may override wavelength in promoting polarized motility. Indeed, examination of cell shape and behavior as a function of wave amplitude showed a step-function response, with elongation, polarization, and migration persistence enhanced at amplitudes below 7.5 μm and inhibited at amplitudes greater than 15 μm (Fig. 2 *H–J* and Movie S7). In contrast to migration directionality, HEY-T30 migration speed was insensitive to waveform (*SI Appendix*, Fig. S1 *G* and *H*). To determine whether the repetitive pattern of aligned waves contributed to the cellular response, we analyzed our data as a function of the nematic order of the fibril-like substrates. This showed that the relationship between substrate nematic order and cell polarization metrics was similar to that seen for substrate wavelength, with a linear increase in cell polarization with increasing nematic order, with the small-wave substrate data also an outlier (*SI Appendix*, Fig. S1 *B–F*). Because all of our cell polarization data, including the small-wave substrates, was best fit by the step-function response seen with increasing wave amplitude, we chose to utilize amplitude as the primary wave variable for further analyses. Importantly, the response required 3D ridge ECM architecture, as two-dimensional (2D) printing of similar wavy collagen patterns interspersed by nonadhesive areas failed to produce a cell elongation response to alterations in wave amplitude (*SI Appendix*, Fig.S1 *I* and *J*). Our results suggest that wavy fibril-like ECMs inhibit cell polarization and migration above a threshold amplitude.

PI3K Promotes Cell Polarization in Response to ECM Waveform Independent of a Cell-Scale PIP3 Gradient. We next sought to determine how cells might detect and translate ECM fibril wave amplitude into polarized cell shape and migration responses. We examined the elongation response to fibril-like wave substrates in cells treated with inhibitors of known migration and polarization pathways, including PIP3 generation, actin polymerization, and myosin contractility (Fig. 3*A*). We first focused on the role of the acidic phospholipid PIP3. Cells plated on wave substrates and treated with 100 nM wortmannin to block PI3K activity were able to adhere, but not elongate or polarize (Fig. 3*A* and *SI Appendix*, Fig. S1 *A–C* and Movie S8). To determine if a PIP3 gradient mediates cell polarization on wave substrates, we analyzed the localization of the PH domain of Akt fused to GFP (GFP-PH-Akt) as a biosensor for PIP3. GFP-PH-Akt polarization was defined as the distance between the centroid of the cell shape and the center of mass GFP-PH-Akt fluorescence, normalized to length of the cell major elliptical axis, such that this number approached zero when fluorescence was distributed symmetrically around the cell and increased when fluorescence was asymmetrically distributed (*SI Appendix*, Fig. S2*D*). The

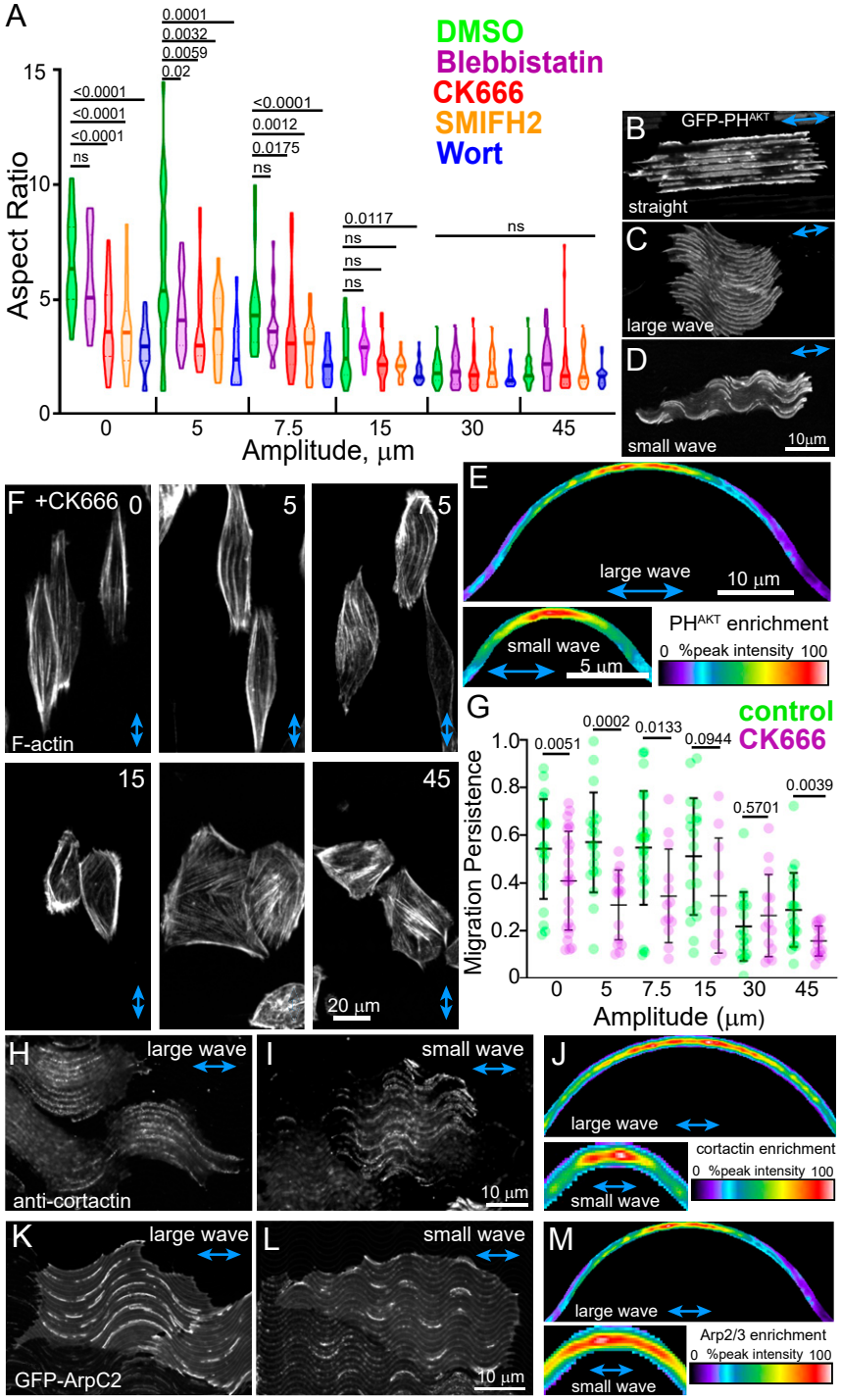

Fig. 3. Lamellipodial machinery responds preferentially to wave curvature, and does not correlate to cell leading edges. (*A*) U2OS cell aspect ratio plotted as a function of substrate wave (fibronectin coated) amplitude (wavelength = 50 μm) for cells treated with DMSO (vehicle, green), 40 μM blebbistatin (purple), 100 mM CK-666, 20 μM SMIFH2, or 50 nM wortmannin. DMSO: $n = 44$, 43, 42, 41, 27, and 27 cells; CK666: $n = 27$, 31, 30, 38, 27, and 22; SMIFH2: $n = 20$, 24, 19, 23, 25, and 33; and wortmannin: $n = 27$, 34, 22, 35, 27, and 17 cells for straight, 5, 7.5, 15, 30, and 45, respectively. SD shown. (*B–D*) confocal images of U2OS cells expressing GFP-PH-Akt adhered to (*B*) straight, (*C*) large-wave, and (*D*) small-wave fibronectin-coated substrates. (*E*) Normalized average intensity ($n = 45$ images) of GFP-PH-Akt along half-wavelengths of (*Upper*) large-wave and (*Lower*) small-waves. (*Inset*) Intensity scale. (*F*) Confocal images of phalloidin-stained actin in CK666- (100 μM) treated U20S cells on collagen-coated wave substrates of constant wavelength (50 μm) and increasing amplitude. (*G*) Migration persistence from time-lapse movies of HEY T30 cells plotted as a function of wave amplitude in the absence (control) or presence of CK666. cells for Control: $n = 20$, 19, 23, 19, 17, and 20 cells for straight, 5, 7.5, 15, 30, and 45, respectively; CK666: $n = 24$, 15, 13, 10, 14, and 16 cells for straight, 5, 7.5, 15, 30, and 45, respectively. SD shown. (*H* and *I*) Confocal images of immunolocalized cortactin in U2OS cells on collagen-coated large- (*H*) or small- (*I*) wave substrates. (*J*) Normalized average intensity ($n = 64$ images) of cortactin along half-wavelengths of (*Upper*) large-wave and (*Lower*) small-wave fibrils. (*Inset*) Intensity scale. (*K* and *L*) Confocal images of GFP-ArpC2 in U2OS cells on large (*K*) or small (*L*) waves. (*M*) Normalized average intensity ($n = 62$ images) of GFP-Arp2 along half-wavelengths of (*Upper*) large-wave and (*Lower*) small-wave fibrils. (*Inset*) Intensity scale. Wave amplitude (μm) denoted upper right. Blue arrows: wave axis.

metric was validated by plating cells on ECM islands of circular or "crossbow" [mimicking a migrating cell (36)] shape (*SI Appendix*, Fig. S2*E*). Surprisingly, this showed intermediate values of GFP-PH-Akt polarization across a range of wave amplitudes that produced varying effects on cell elongation and polarization (*SI Appendix*, Fig. S2*E*). Thus, although PI3K activity is required for cell polarization induced by low-amplitude ECM fibril-like waves, polarization is independent of a cellular PIP3 gradient.

To determine whether PIP3 responds to local aspects of waveform, we examined the distribution of GFP-PH-Akt along single-wave ridges. For cells on straight ridges, GFP-PH-Akt was localized along ridges across the cell length (Fig. 3*B*). In contrast, in cells on wavy substrates, GFP-PH-Akt concentrated at curved wave peaks, and was depleted from straighter segments between peaks (Fig. 3 *C* and *D*). This was validated by averaging the distribution of GFP-PH-Akt across many single half-wavelengths for large-wave and small-wave substrates (Fig. 3*E*). Together, these results show that although the curvature of fibril-like ECM waves mediates local accumulation of PIP3, PI3K promotes cell polarization response to waveform independent of a cell-scale PIP3 gradient.

Lamellipodial Actin Assembly Machinery Localizes to Wave Curvature, Not Cell Leading Edges. We next sought to determine if cell polarization response to waveform was mediated by polarized lamellipodial actin assembly. Inhibition of the Arp2/3 complex with CK-666 elicited a small but significant reduction in U20S cell elongation and HEY T30 directional migration induced by low-amplitude wave substrates (Fig. 3 *A*, *F*, and *G* and Movie S9). We analyzed the localization of the Arp2/3 recruiter cortactin by immunofluorescence (Fig. 3 *H* and *I*), GFP-Arp2 was expressed as a marker of Arp2/3 (Fig. 3 *K* and *L*), and assembly-competent free "barbed" ends of actin filaments (*SI Appendix*, Fig. S2 *F–I*) were localized by permeabilization in the presence of fluorescent monomeric actin. Similar to PIP3 biosensor localization, lamellipodial actin assembly markers did not localize along the leading edges of elongated cells on small-wave substrates, but concentrated at wave peaks in both polarized cells on small-wave substrates and depolarized cells on large-wave substrates (Fig. 3 *J* and *M*). In addition to wave peaks, free barbed ends also localized to FA-like elongated plaques along the straight segments on the "shoulders" of ECM waves and at cell edges. Notably, treatment with CK-666 abolished barbed ends at wave peaks, but not at FAs (*SI Appendix*, Fig. S2*I*). These results indicate that polarity signaling and lamellipodial actin assembly machinery respond to curvature of fibril-like ECM structures, and although required for polarized motility, do not localize to leading edges of polarized, directionally migrating cells.

FA Orientation and Maturation Correlates with Cell Polarization and Migration on ECM Waves. We next sought to determine the role of integrin engagement and FA organization in cell shape and migratory responses to ECM fibril waveform. Plating U2OS cells on ECM fibril substrates coated with collagen, fibronectin, or concanavalin-A (to promote adhesion without integrin engagement) showed that cell elongation response to low-amplitude ECM fibril waves was integrin-dependent, but not ECM receptor-specific (Fig. 4 *A* and *B*). Fibroblasts from FAK$^{-/-}$ or wild-type mouse embryos showed that compared to wild-type, FAK-null cells showed a small but significant decrease in cell elongation on straight or low-amplitude waves, suggesting that although not required, integrin signaling through FAK enhances cell polarization on low-amplitude wave substrates. Paxillin localization showed that in cells on straight ECM ridge substrates, FAs were localized to leading cell edges and along ridges in the cell body (35, 39) (Fig. 4*E*). In depolarized cells on large-wave substrates, FAs localized mostly along wave peaks (Fig. 4 *F* and *H*), while in polarized cells on small-wave substrates, FAs were absent from wave peaks, but localized to peak shoulders and cell leading edges (Fig. 4 *G* and *H*). Line-scan analysis showed that FAs in cells on straight or small-wave substrates were elongated (mature) FAs, whereas those at peaks of large waves were closely spaced series of small (nascent) FAs (Fig. 4 *I*, *K*, and *L*). Because paxillin concentrates at FA ends near the leading edge and zyxin at the stress fiber–FA junction (40) (Fig. 4 *M–O*), we measured FA orientation as the angle of a line defined by the peak fluorescence intensities of paxillin and zyxin coimmunostaining within each FA relative to the wave axis. In cells on straight ECM ridges, the paxillin-zyxin axis of FAs was aligned parallel to the ridges, as expected. In cells on large-wave substrates, FAs were oriented near perpendicular (greater than ±45°) to the wave axis (Fig. 4 *P–R*). In contrast, in cells on small-wave substrates, FAs were never perpendicular, but were oriented closer to parallel (±30°) to the wave axis. Thus, the fibril-like ECM waveform regulates FA maturation and orientation, and FA orientation correlates with the polarization and directional migration response of cells to the waveform.

ECM Waveform Dictates Stress Fiber Bending and Length. Because FAs mature via actomyosin stress fiber contractility, we hypothesized that stress fibers may be organized downstream of FA orientation to mediate the cellular polarity and motility responses to ECM waveform. Inhibition of formin-family actin nucleators with SMIFH2 blocked stress fiber formation and caused a small but significant reduction in U2OS cell elongation induced by low-amplitude substrate waves (Fig. 3*A*). Quantification of stress fiber coalignment ("anisotropy") (Fig. 5*B*) (41) and alignment relative to the wave axis (Fig. 5*C*) showed that in cells on straight and low-amplitude substrates, actin bundles were highly anisotropic and tightly oriented along the wave axis. In contrast, in cells on high-amplitude waves, bundle anisotropy decreased and the distribution of stress fiber orientation relative to the wave axis broadened and the average angle increased (Fig. 5*C*). Thus, the coalignment and orientation of formin-mediated actin stress fibers correlate with the polarization and directional migration responses of cells to ECM waveform.

We next sought to determine how fibril-like ECM waves regulate stress fiber orientation and alignment. We used confocal polarization microscopy to examine filament coalignment and continuity within stress fibers in U2OS cells on straight, small-, and large-wave substrates. This showed that well-aligned actin filaments in bundles transitioned smoothly in orientation around wave peaks on large-wave ECMs (Fig. 5*D*), but exhibited discontinuities or splaying on small-wave ECMs (Fig. 5*D*). Three-dimensional confocal analysis showed that stress fiber length depended on waveform and depth from the cell surface (Fig. 5 *F–H*). In cells on straight fibril-like ridges, cortical bundles in the *z*-plane at the ventral cell surface and subcortical bundles deeper in the cell both spanned the full cell length along ECM ridges (Fig. 5 *F* and *F′*). At the ventral surface of cells on small-wave substrates, short, cortical stress fibers either were aligned along the straight segments of waves at an angle to the wave axis, consistent with the localization of FAs, or were discontinuous where they bent around wave peaks (Fig. 5 *E*, *H*, and *I*). However, deeper in these cells, long continuous subcortical stress fibers aligned along the wave axis and spanned the cell end-to-end, over the tops of wavy ECM fibrils (Fig. 5 *H′* and *I′*). In cells on large-wave substrates, cortical actin at the ventral surface formed bundles that followed the curve of the waves, bending around the peaks (Fig. 5*G*). Deeper in these cells, shorter, continuous subcortical bundles spanned half-wavelengths forming "chords," but did not span the full cell length (Fig. 5*G′*). Thus, large-amplitude wave fibril-like ECMs drive cortical actin bundles to bend around wave peaks, and this behavior correlates with FA orientation perpendicular to wave axis and cell depolarization. In contrast, small-amplitude waves

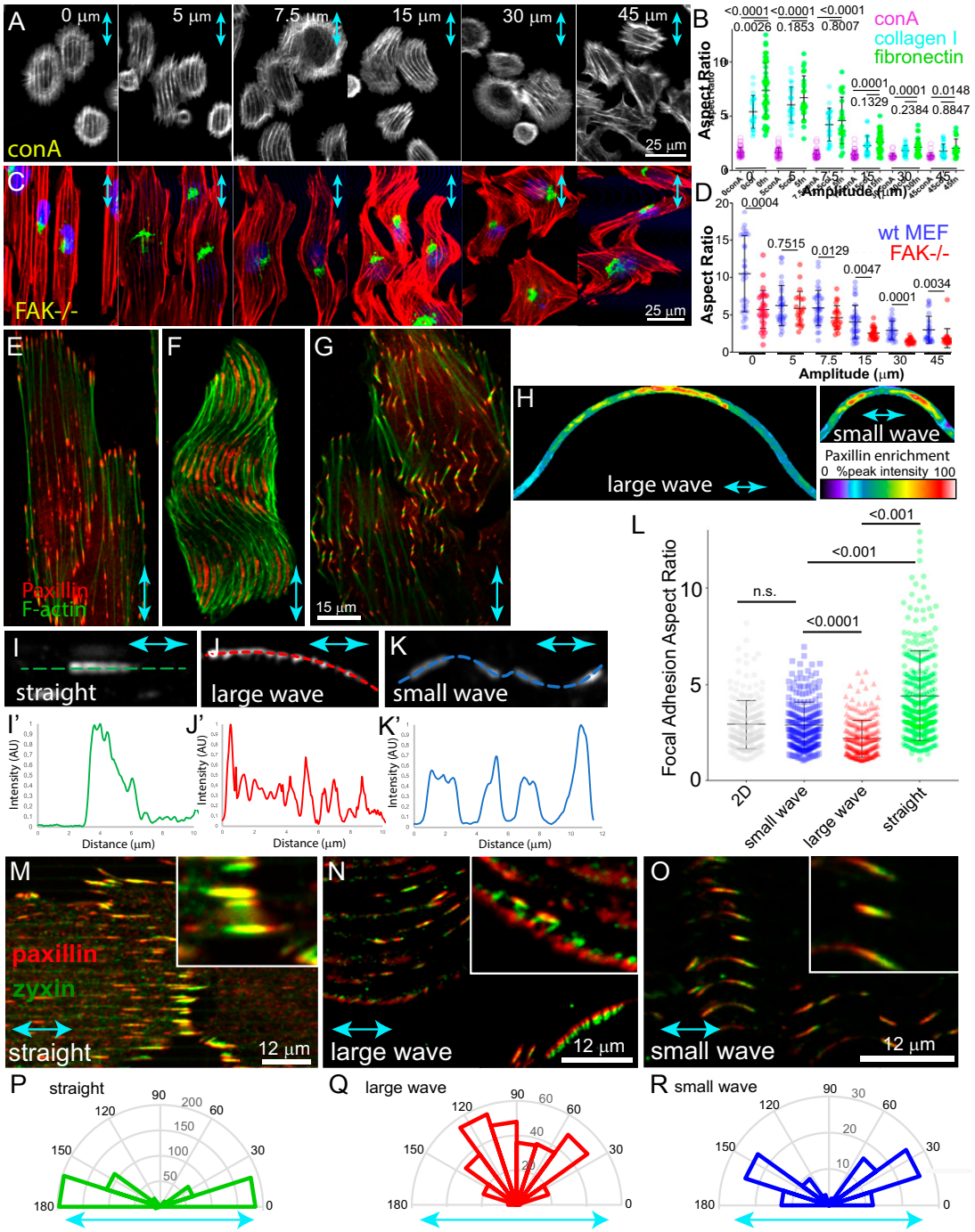

Fig. 4. FA orientation and maturation correlates with cell polarization and migration on ECM waves. Imaging and analysis of (*A*, *B*, and *E*–*R*) U2OS cells and (*C* and *D*) fibroblasts on fibronectin wave substrates. Confocal images of (*A*) U2OS cells and (*C*) FAK$^{-/-}$ fibroblasts with phalloidin-stained actin (red), GM130 (green), and DAPI-stained DNA (blue), on wave substrates with a wavelength of 50 μm and increasing amplitude, coated with (*A*) concanavalin A (conA) or (*C*) fibronectin. Aspect ratio of (*B*) U20S cells and (*D*) fibroblasts as a function of wave amplitude. In *B*, substrates were coated with conA, collagen, or fibronectin:, conA: $n = 44$, 43, 42, 41, 27, and 27 cells for straight, 5, 7.5, 15, 30, and 45, respectively; collagen: $n = 22$, 24, 21, 21, 20, and 21 cells for straight, 5, 7.5, 15, 30, and 45, respectively; fibronectin: $n = 27$, 34, 21, 35, 27, and 17 cells for straight, 5, 7.5, 15, 30, and 45, respectively. *Upper P* value: = Mann–Whitney test between fibronectin and ConA; *Lower* value: same test between fibronectin and collagen. In *D*, substrates were coated with fibronectin, FAK$^{-/-}$: $n = 31$, 33, 35, 35, 26, and 27 cells for straight, 5, 7.5, 15, 30, and 45, respectively; wild-type MEFs: $n = 29$, 21, 23, 25, 23, and 19 cells for straight, 5, 7.5, 15, 30, and 45, respectively. (*E*–*S*) U20S cells plated on fibronectin-coated ECM fibril wave substrates ((*E*, *I*, *I′*, and *G*) straight, (*G*, *H*, *K*, *K′*, and *O*) small-wave, and (*F*, *H*, *J*, *N*, and *R*) large-wave substrates. (*E*–*G*) Immunolocalization of paxillin (red) and phalloidin (green) staining of actin. (*H*) Normalized average paxillin intensity ($n =$ 41 and 105 images for large and small waves, respectively) along half-wavelengths of (*Left*) large wave and (*Right*) small waves. (*I*–*K*) Immunolocalization of paxillin and (*I*–*K*) line scans. (*L*) Aspect ratio of paxillin-labeled FAs in cells plated on fibronectin-coated coverslips (2D) or wave substrates, each point represents one FA. 2D: $n = 216$; small wave; $n = 249$; large wave: $n = 255$; straight; $n = 282$. (*M*–*O*) Coimmunolocalization of zyxin (green) and paxillin (green). *Insets* show 2.75× magnification of adhesions. (*P*–*R*) Radial histograms of FA orientation, defined as the angle of a line between the peak fluorescence intensities of paxillin and zyxin staining within each FA relative to the wave axis. Straight: $n = 88$; large wave: $n = 92$; small wave; $n = 78$. Wave amplitude in upper right. Blue arrows: wave axis. Long bars = mean; short bars = SD.

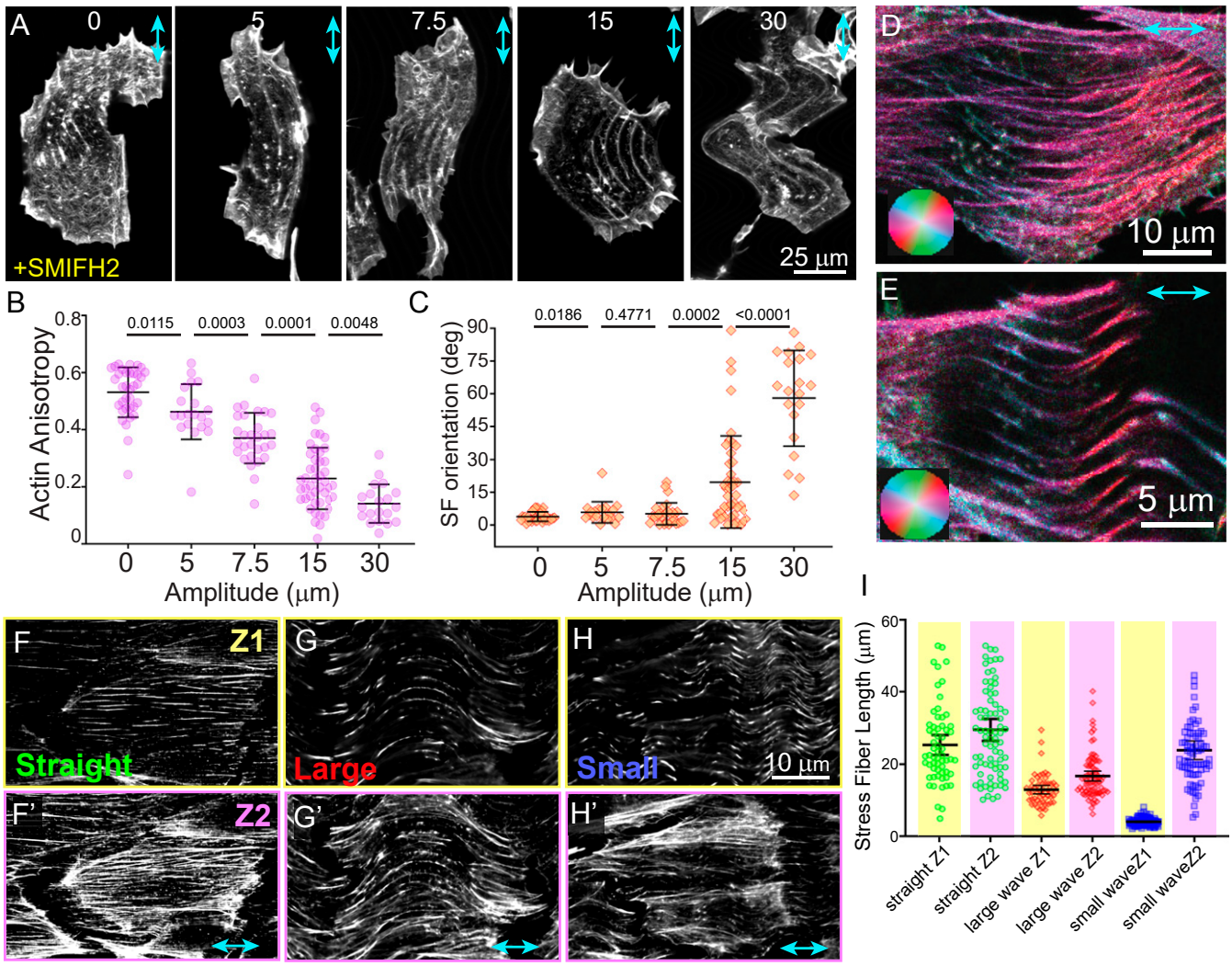

Fig. 5. ECM waveform dictates stress fiber bending and length. Imaging and analysis of U2OS cells on fibronectin-coated wave substrates. (*A*) Confocal images of phalloidin-stained actin in cells on wave substrates of 50-μm wavelength and increasing amplitude in the absence (control) or presence of 20 μM SMIFH2. (*B*) Average stress fiber coalignment (actin anisotropy) and (*C*) stress fiber alignment relative to the fibril wave axis (SF orientation), as a function of wave amplitude. (*B*) $n = 35$, 20, 29, 45, and 20 cells for straight, 5, 7.5, 15, and 30, respectively; (*C*) $n = 35$, 20, 29, 45, and 30 cells for straight, 5, 7.5, 15 and 30, respectively. Long bars = mean, short bars = SD, Mann–Whitney tests shown. (*D* and *E*) Three-dimensional confocal polarization image of phalloidin-stained actin. Color: F-actin anisotropy orientation (color-wheel *Inset*) saturation: anisotropy, white = isotropic. (*F–H′*) Confocal images of phalloidin-stained actin (*F–H*, yellow box, Z1) at the ventral cell surface and (*F′–H′*, pink box, Z2) ~1 μm above the ventral cell surface. (*I*) Average stress fiber length measured at Z1 and Z2. $n = 61$ and 80 for straight, Z1 and Z2, respectively; 55 and 83 for large-wave, Z1 and Z2, respectively; 97 and 75 for small-wave, Z1 and Z2, respectively. Wave amplitude, upper right. Blue arrows: wave axis. Long bars = mean; short bars = 95% confidence intervals.

limit cortical bundle length at the ventral cell surface either by FA formation on wave shoulders or bundle breakage at wave peaks, but permit long, subcortical bundles to form over the top of fibril-like waves, presumably allowing integration of cytoskeletal forces across the cell and along the wave axis.

ECM Wave Amplitude Dictates Actomyosin Flow Orientation to Mediate Cell Polarization. Because stress fiber and FA organization are determined by myosin II-mediated contractility (42–44), we hypothesized that myosin II could regulate these functions in response to fibril-like ECM waveforms. Analysis of myosin IIA [tagged on N and C termini with GFP and mApple (45, 46)] organization in U2OS cells on wave substrates showed that minifilaments localized periodically along all stress fibers, both cortical and subcortical, in cells on both small- and large-wave substrates. However, on large-wave substrates, myosin IIA additionally localized to a subcortical actin meshwork that bridged between stress fibers bent around wave peaks and chords at wave bases, where it formed "ribbons" of laterally aligned minifilaments (*SI Appendix*, Fig. S2*J*), reminiscent of myosin II organization in the lamella of cells migrating on planar ECMs (47–49). Coupled with the localization of PIP3, Arp2/3, and FAs at wave peaks and myosin II ribbon structures behind the peaks, these observations suggest that large-wave fibril-like substrates induce the formation of "cryptic leading edges" that could orient FAs through cytoskeletal retrograde flow.

To test whether actomyosin retrograde flow mediates cell-polarization responses to wave amplitude, we analyzed GFP-myosin IIA dynamics in U2OS cells plated on large-and small-wave substrates. Time-lapse movies showed that for cells on large-wave substrates, myosin IIA minifilaments formed near wave peaks at the cell periphery and flowed centripetally, perpendicular to the wave axis, eventually condensing into the subcortical chord stress fibers that spanned half-wavelengths

(Fig. 6 *A* and *B* and Movie S11), similar to actomyosin dynamics in the lamella of cells migrating on planar ECMs (49). Cells spanning a full wavelength thus exhibited two spatially offset and opposing myosin II flow-fields that ran perpendicular to the wave axis and whose length and width were determined by the wavelength and wave amplitude, respectively. In contrast, for cells plated on small-wave substrates, actomyosin flow perpendicular to the wave axis also occurred centripetally from peripheral wave peaks. However, because the distance of retrograde flow was limited by the small-wave amplitude, the flow from each peak collapsed quickly into long subcortical stress fibers that spanned multiple wavelengths along the wave axis (Fig. 6 *C* and *D* and Movie S12). Flow was then dominated by the contractile motion along these stress fibers from each pole of the elongated cell toward its center. Together, these results suggest that curvature of wavy ECM fibrils localizes PIP3 to wave peaks to direct local actomyosin assembly and retrograde flows, that, in turn, drive FA formation, orientation, and maturation to establish actin stress fibers, whose length and organization is dictated by flow-dependent interaction with fibril-like waveforms to determine cell polarization and migration responses.

Myosin Contractility Regulates Cancer Cell Polarization and Migration Responses to ECM Waveform. Given our finding that actomyosin organization and dynamics determines cell migration responses to the ECM waveform, we postulated that the intrinsic level of contractility could dictate cancer cell migration ability on ECM wave substrates. To test this, we first measured and ranked several cancer cell lines and mouse embryo fibroblasts (MEF) based on their level of phosphorylated myosin II regulatory light chain (pMRLC) as a proxy for intrinsic actomyosin activity. This showed a range of pMRLC levels as follows: HEY T30 < U2OS < MB231 (breast cancer) < MEF <SKOV3 (ovarian cancer) (Fig. 6 *E* and *F*). Analysis of cell elongation in response to a range of ECM wave amplitudes revealed that low-contractility U2OS and HEY T30 cells polarized on wave amplitudes of 7.5 μm or less, while more highly contractile MEF polarized on amplitudes of 15 μm or less (Fig. 6*G*). Consistent with this, the directional persistence of cell migration on 15-μm amplitude waves was higher in high-contractility SKOV3 than in lower contractility HEY T30 or MB-231 cells (Fig. 6*H* and Movie S13). We then manipulated myosin II activity directly to determine if changes in contractility were sufficient to regulate cellular responses to the ECM waveform. Treatment with blebbistatin reduced the depolarization threshold of U2OS cells from 7.5- to 5-μm amplitude waves (Figs. 3*A* and 6*I* and *SI Appendix*, Fig. S2*K*) and decreased migration persistence of MB-231 cells on low-amplitude waves (Fig. 6*J* and Movie S10). Conversely, overexpression of mEmerald-myosin IIA in HEY T30 cells increased their wave amplitude depolarization threshold from 7.5 to 15 μm (Fig. 6*K*). Thus, the contractility level of cancer cells is sufficient to determine their ability to polarize and migrate on wavy ECM fibril-like substrates, with higher contractility promoting cell polarization across a broader range of ECM waveforms.

Discussion

Our work shows that ECM wave architecture regulates contact guidance of tumor cells via actomyosin contractility, and suggests that oncogenic modulation of cell contractility may dictate the range of ECM waveforms that are conducive to metastatic cell migration. The stromal ECM of healthy tissue consists of a wavy meshwork of collagen bundles, which is altered by conditions such as obesity, where stromal bundles are straighter (13). In cancer, it is generally accepted that the ECM around tumors acts as a barrier through which tumor cells must travel in order to metastasize. Proteolysis and remodeling of the wavy meshwork into straighter bundles that radiate from the tumor by cancer and immune cells and associated fibroblasts is thought to promote cell dispersion (50). We tested the hypothesis that linear collagen fibrils, such as those seen in obese mammary tissue and the tumor microenvironment, promote contact guidance-mediated cancer cell migration, while wavy ECM fibrils typical of healthy stroma inhibit migration. We found in mouse and human tissues (7) that collagen fibrils exhibit wave-like forms that vary as a function of location in the tumor microenvironment, tissue adipose level, or tumor grade, with tumor cores, obese tissue, and high-grade tumors displaying ECM fibril waveforms of low amplitude and wavelength, and tumor periphery, lean stroma, and low-grade tumors displaying ECM fibril waveforms of high amplitude and wavelength. Nanotopographic ECM-coated substrates with features that approximated the ECM fibril size and the range of waveforms observed in vivo demonstrated waveform-dependent polarization and migratory responses in cancer cells, with cell polarization and directional migration promoted below a threshold of wave amplitude, and depolarization and poor migration above that threshold. We propose that in addition to a physical barrier, wavy ECM bundles serve as a "cell polarization barrier," with high-amplitude waves depolarizing tumor cells and preventing their directional migration and dissemination. However, we further discovered that cancer cells of different intrinsic contractility depolarized at different ECM wave amplitudes, and that we could tune cell polarization on wavy ECM substrates by manipulating contractility. Although tumor ECM architecture has been suggested to be predictive of cancer outcome (51), our results suggest that oncogenic upregulation of contractility could drive cell dissemination even on wavy collagen bundles typical of noncancerous stroma. Thus, ECM architecture and myosin II activation level should be weighed in tandem in considering the predictive value of microenvironmental ECM architecture in cancer progression.

Contact guidance is a powerful polarization cue that can affect all cell types studied to date (52). Our data extend those observations, showing that wavy topographic ECM fibril-like substrates also regulate polarization of all cell types investigated. Our study suggests a mechanistic model for how ECM fibril waveform dictates the organization and dynamics of the actomyosin cytoskeleton to determine whether cells undergo contact guidance-mediated migration or are blocked from migration by cell depolarization (Fig. 6*L*). We found that migration on low-amplitude ECM waves required PI3K and integrin signaling, as well as Arp2/3, formin, and myosin II activities, similar to planar ECMs. However, polarization signaling and lamellipodial actin assembly machinery did not localize to leading edges in the direction of cell migration along the wave axis, but concentrated at wave peaks. PI3K signaling thus likely responds to local plasma membrane curvature induced by membrane adhesion to curved regions of fibril-like ECM ridges at wave peaks. Membrane curvature may be sensed by I-BAR domain-containing proteins (53), such as IRSp53, that could recruit and activate Rac1 to initiate lamellipodia actin and myosin II filament polymerization and nascent FA assembly (54–56). As such, each wave peak along the cell edge creates a "cryptic leading edge" oriented perpendicular to the wave axis.

Although these cryptic leading edges are not oriented with migration, they still mediate cell polarization and migration through their role in organizing actomyosin dynamics to direct FA maturation and stress fiber orientation. Arp2/3-mediated actin polymerization against the plasma membrane within each cryptic lamellipodium drives local actin retrograde flow, while myosin II contraction remodels this dendritic network into contractile arcs by a network-contraction mechanism (47, 49). Arcs undergo retrograde flow until reaching the base of the wave, where they form chords that span half-wavelengths. In cells on high-amplitude or large ECM fibril waves, as arcs undergo retrograde flow over the distance of the wave amplitude, myosin

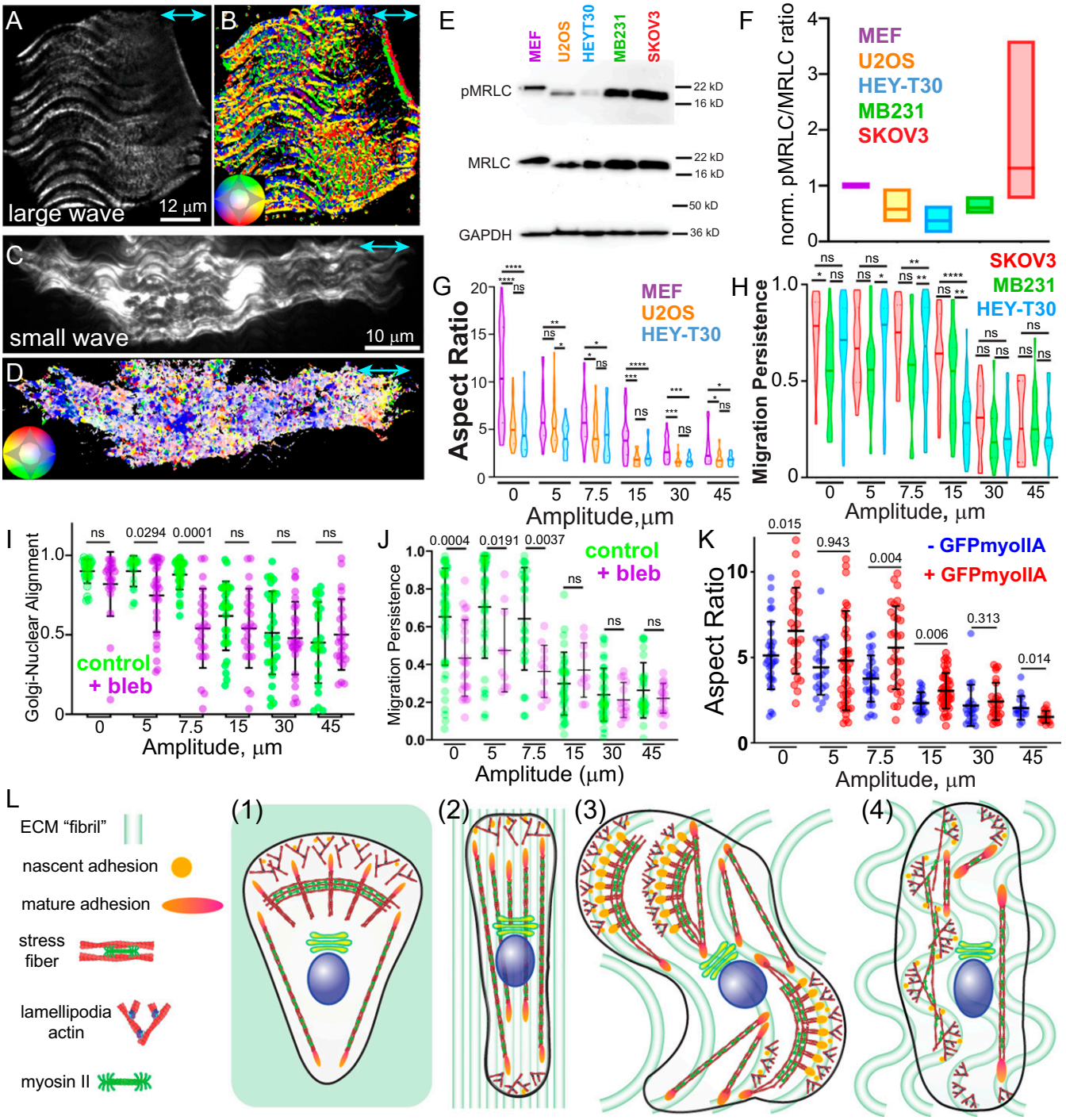

Fig. 6. Actomyosin contraction is organized by ECM waves and determines cell polarization response. (*A* and *C*) Confocal images from time-lapse series of U2OS cells expressing GFP-myosin IIA plated on fibronectin-coated large (*A*) or small (*C*) wave substrates (Movies S12 and S13). (*B* and *D*) Color-encoded directional flow map of myosin IIA filament dynamics from analyses of time-lapse image series of the cells in *A* and *C*, *Inset*. Color legend for flow direction. (*E*) Western blot of MRLC phosphorylated on serine 19 (pMRLC), MRLC, and GAPDH from lysates of cell types noted. (*F*) Quantification of normalized pMRLC:MRLC ratios from Western blots, $n = 4$ experiments, range and median shown. (*G*) Aspect ratio and (*H*) cell migration persistence as a function of substrate wave amplitude for cell types noted. (*I*) U2OS cell polarization as measured by Golgi-nucleus alignment to ECM fiber wave direction plotted as a function of amplitude in (purple) the presence and (green) the absence of 40 μM blebbistatin. (*J*) Migration persistence of MB231 cells in the presence or absence of blebbistatin. Control: $n = 48$, 35, 26, 32, 35 and 26 cells for straight, 5, 7.5, 15, 30, and 45, respectively; blebbistatin: $n = 24$, 10, 11, 10, 14 and 16 cells for straight, 5, 7.5, 15, 30, and 45, respectively. (*K*) Aspect ratio as a function of substrate wave amplitude in HEY T30 cells with (+GFPmyoIIA) or without (−GFPmyoIIA) overexpression of GFP-myosin IIA. Control: $n = 27$, 21, 26, 26, 16, and 17; +GFP-myosinIIA: 26, 42, 31, 44, 26, 17 cells for straight, 5, 7.5, 15, 30, and 45, respectively. For statistical comparisons (*Materials and Methods*), ****$P < 0.0001$, ***$P \leq 0.001$, **$P \leq 0.01$, *$P \leq 0.05$, and ns is not significant. Blue arrows: wave axis. Long bars = mean; short bars = SD. (*L*) Speculative model for mechanism of cellular response to ECM waves. 1) Model for cell on 2D substrate, 2) model for cell on linear ECM ridges, 3) model for cell on large-wave ECM ridges, and 4) model for cell on small-wave ECM ridges. See *Discussion* for details.

II continues to accumulate to strengthen the arcs and build "ribbons" of aligned minifilaments (Fig. 6 *L*, *3*), resembling the lamella of migrating cells on planar ECMs (45, 46) (Fig. 6 *L*, *1*). Contraction and retrograde flow in these cryptic lamellae pull on actin linked to FAs along the wave peak to orient the FAs perpendicular to the wave axis and thus cause cell depolarization. In contrast, in cells on small ECM fibril waves, the distance of retrograde flow from cryptic leading edges at wave peaks is limited by the small-wave amplitude. This short distance limits the amount of time that myosin II accumulates on the actin network, and thus the cryptic leading edges do not develop into contractile lamellae. Small contractile bundles form, but are either too short to generate arcs, are weak and get broken while bending around the ECM fibril wave peaks, or slip over low-amplitude wave peaks and form chords at the base of waves that coalesce into long, contractile stress fibers spanning multiple wavelengths (Fig. 6 *L*, *4*). These long stress fibers act to orient FAs and integrate cytoskeletal forces along the wave axis to drive directed cell migration. This results in linearly oriented adhesions, stress fibers, and contraction, as observed in straight ECM fibers (Fig. 6 *L*, *2*), and thus similarly directed cell migration.

The role of actomyosin contractility in promoting tumor cell metastasis has been controversial. In many types of solid tumors, increased ECM stiffness correlates with tumor progression and enhanced cell migration via actomyosin-mediated mechanosensation (57–59). However, whether more aggressive tumor cells necessarily have enhanced contractility is less clear. In ovarian cancer, tumor cell stiffness and invasion are inversely correlated in vitro (60), and metastatic tumor cells are softer than benign cells (61), suggesting that actomyosin contractility may be lower in more aggressive tumor cells. However, cell stiffness is not necessarily a proxy for contractility. For example, the anticancer drug cisplatin increases cell stiffness and decreases invasion independent of contractility but dependent on F-actin (62, 63). Furthermore, other studies show Rho/ROCK-mediated contractility in tumor cells correlates with enhanced migration (64, 65), invasion (66), intravasation, survival in the blood stream, and metastasis (64). Contractility also can promote tumor cell motility and metastasis via adhesion-independent amoeboid migration (67–71). Actomyosin activity can drive bundle formation, which is necessary for both amoeboid migration (70) and for navigating curved ECM fibril environments. Thus, together with our findings, this suggests further study of the predictive value of myosin II activity in cancer prognosis would be valuable.

Materials and Methods

Antibodies and Reagents. For detailed reagent listings, see *SI Appendix, Supplemental Materials & Methods*.

Cell Lines and Culture. Cell culture was performed via established methods. For individual cell line protocols, see *SI Appendix*.

Nanotopographic Substrates. Nanotopographic were fabricated as previously described (38). For more detailed description, see *SI Appendix, Supplemental Materials & Methods*.

Mouse Tumor Models. Mouse tumor and stroma were imaged essentially as previously described (13); additional details are available in *SI Appendix*. Animal protocols and care were approved by the Institutional Animal Care and Use Committees at the National Heart Lung and Blood Institute or Cornell University.

Imaging. Various previously described imaging modalities were used, including spinning-disk confocal microscopy, second harmonic imaging, 3D STED, and scanning-electron microscopy. Full details for each are in *SI Appendix*.

Confocal Fluorescence Polarization. Confocal fluorescence polarization images of phalloidin labeled F-actin were acquired with Zeiss LSM 780 adapted with a liquid crystal-based polarization modulator. Confocal polarization data were acquired by switching the polarization state of the excitation laser using a liquid crystal universal compensator (sandwich of two variable retarder plates without a polarizer; Meadowlark Optics Inc.). This method is an adaptation of excitation-resolved fluorescence polarization imaging in transmission (72) and emission-resolved instant fluorescence polarization imaging in reflection (73). Confocal fluorescence polarization was employed for analysis of F-actin orientation (74). Briefly, the polarization state of the laser was calibrated against a rotating polarizer placed on the stage, using the calibration process used for instant fluorescence polarization microscope (73). The universal compensator was programmed to produce four excitation polarization orientations (0, 45, 90, 135). A redundant image at 0° orientation was acquired to account for photobleaching. Images were collected using the Zen Black software equipped with a Visual Macro Editor. We used a custom MicroManager plugin (OpenPolScope.org) to control the liquid crystal in response to the images produced by Zen Black software. Polarization-resolved images were background-corrected and used to retrieve fluorescence intensity, anisotropy, and orientation using the MATLAB code used for analysis of instant fluorescence PolScope (https://github.com/mehta-lab/Instantaneous-PolScope).

Cell Fixation and Immunofluorescence. Cell fixation and immunofluorescence was performed as previously described (43). For full details, see *SI Appendix*.

Western Blotting. Western blotting was performed essentially as described previously (43). For full details, see *SI Appendix*.

ECM Micropatterning. To create 2D micropatterns of ECM proteins on coverslips with equivalent waveforms to those produced by 3D nanotopography, Alexa 647-labeled fibronectin was deposited in patterns created by a PRIMO DMD micropatterning device (Alveole), as previously described (75). Further details are provided in *SI Appendix*.

Image Analysis. Image analyses were performed using ImageJ and Metamorph packages, For detailed descriptions of each analysis, see *SI Appendix*.

Statistical Analyses and Presentation. Statistical analysis for each data set was performed using GraphPad Prism. Details are given in *SI Appendix*.

Data Availability. All study data are included in the article and supporting information.

ACKNOWLEDGMENTS. We thank the National Heart, Lung, and Blood Institute Light Microscopy Core Facility for assistance with stimulated emission depletion and second harmonic-generation imaging; and Arezki Boudaoud for helpful discussions on nematic order. This work was supported by the Division of Intramural Research, National Heart, Lung, and Blood Institute (R.S.F., M.A.B. and C.M.W.) and National Cancer Institute Grant 1U54CA210184 (to B.R.S. and C.F.). J.T.F., X.S., M.J.H., and W.L. were supported by Air Force Office of Scientific Research Grant FA9550-16-1-0052. M.J.H. received partial support from the National Cancer Institute–University of Maryland Partnership for Integrative Cancer Research and NSF Grant PHY 1806903.

1. N. I. Nissen, M. Karsdal, N. Willumsen, Collagens and cancer associated fibroblasts in the reactive stroma and its relation to cancer biology. *J. Exp. Clin. Cancer Res.* **38**, 115 (2019).
2. R. Afik *et al.*, Tumor macrophages are pivotal constructors of tumor collagenous matrix. *J. Exp. Med.* **213**, 2315–2331 (2016).
3. P. P. Provenzano *et al.*, Collagen density promotes mammary tumor initiation and progression. *BMC Med.* **6**, 11 (2008).
4. K. R. Levental *et al.*, Matrix crosslinking forces tumor progression by enhancing integrin signaling. *Cell* **139**, 891–906 (2009).
5. A. Kaur *et al.*, Remodeling of the collagen matrix in aging skin promotes melanoma metastasis and affects immune cell motility. *Cancer Discov.* **9**, 64–81 (2019).
6. K. B. Tilbury *et al.*, Stromal alterations in ovarian cancers via wavelength dependent second harmonic generation microscopy and optical scattering. *BMC Cancer* **17**, 102 (2017).
7. B. Wen *et al.*, 3D texture analysis for classification of second harmonic generation images of human ovarian cancer. *Sci. Rep.* **6**, 35734 (2016).
8. T. T. Chang, D. Thakar, V. M. Weaver, Force-dependent breaching of the basement membrane. *Matrix Biol.* **57-58**, 178–189 (2017).

9. M. W. Conklin *et al*., Collagen alignment as a predictor of recurrence after ductal carcinoma in situ. *Cancer Epidemiol. Biomarkers Prev.* **27**, 138–145 (2018).
10. P. P. Provenzano *et al*., Collagen reorganization at the tumor-stromal interface facilitates local invasion. *BMC Med.* **4**, 38 (2006).
11. A. S. G. Curtis, M. Varde, Control of cell behavior: Topological factors. *J. Natl. Cancer Inst.* **33**, 15–26 (1964).
12. S. Alkmin *et al*., Migration dynamics of ovarian epithelial cells on micro-fabricated image-based models of normal and malignant stroma. *Acta Biomater.* **100**, 92–104 (2019).
13. B. R. Seo *et al*., Obesity-dependent changes in interstitial ECM mechanics promote breast tumorigenesis. *Sci. Transl. Med.* **7**, 301ra130 (2015).
14. S. J. Heasman, L. M. Carlin, S. Cox, T. Ng, A. J. Ridley, Coordinated RhoA signaling at the leading edge and uropod is required for T cell transendothelial migration. *J. Cell Biol.* **190**, 553–563 (2010).
15. A. J. Ridley, Life at the leading edge. *Cell* **145**, 1012–1022 (2011).
16. P. Devreotes, A. R. Horwitz, Signaling networks that regulate cell migration. *Cold Spring Harb. Perspect. Biol.* **7**, a005959 (2015).
17. A. Rahman, J. M. Haugh, Deactivation of a negative regulator: A distinct signal transduction mechanism, pronounced in Akt signaling. *Biophys. J.* **107**, L29–L32 (2014).
18. S. B. Asokan *et al*., Mesenchymal chemotaxis requires selective inactivation of myosin II at the leading edge via a noncanonical PLCγ/PKCα pathway. *Dev. Cell* **31**, 747–760 (2014).
19. F. K. Mardakheh, A. Self, C. J. Marshall, RHO binding to FAM65A regulates Golgi reorientation during cell migration. *J. Cell Sci.* **129**, 4466–4479 (2016).
20. E. Pallesi-Pocachard *et al*., Hook2, a microtubule-binding protein, interacts with Par6α and controls centrosome orientation during polarized cell migration. *Sci. Rep.* **6**, 33259 (2016).
21. J. Block *et al*., FMNL2 drives actin-based protrusion and migration downstream of Cdc42. *Curr. Biol.* **22**, 1005–1012 (2012).
22. T. D. Pollard, G. G. Borisy, Cellular motility driven by assembly and disassembly of actin filaments. *Cell* **112**, 453–465 (2003).
23. B. J. DuChez, A. D. Doyle, E. K. Dimitriadis, K. M. Yamada, Durotaxis by human cancer cells. *Biophys. J.* **116**, 670–683 (2019).
24. A. Elosegui-Artola, X. Trepat, P. Roca-Cusachs, Control of mechanotransduction by molecular clutch dynamics. *Trends Cell Biol.* **28**, 356–367 (2018).
25. L. B. Case, C. M. Waterman, Integration of actin dynamics and cell adhesion by a three-dimensional, mechanosensitive molecular clutch. *Nat. Cell Biol.* **17**, 955–963 (2015).
26. G. Giannone *et al*., Periodic lamellipodial contractions correlate with rearward actin waves. *Cell* **116**, 431–443 (2004).
27. G. Giannone, G. Jiang, D. H. Sutton, D. R. Critchley, M. P. Sheetz, Talin1 is critical for force-dependent reinforcement of initial integrin-cytoskeleton bonds but not tyrosine kinase activation. *J. Cell Biol.* **163**, 409–419 (2003).
28. P. Naumanen, P. Lappalainen, P. Hotulainen, Mechanisms of actin stress fibre assembly. *J. Microsc.* **231**, 446–454 (2008).
29. V. Swaminathan *et al*., Actin retrograde flow actively aligns and orients ligand-engaged integrins in focal adhesions. *Proc. Natl. Acad. Sci. U.S.A.* **114**, 10648–10653 (2017).
30. N. Q. Balaban *et al*., Force and focal adhesion assembly: A close relationship studied using elastic micropatterned substrates. *Nat. Cell Biol.* **3**, 466–472 (2001).
31. E. J. Ezratty, M. A. Partridge, G. G. Gundersen, Microtubule-induced focal adhesion disassembly is mediated by dynamin and focal adhesion kinase. *Nat. Cell Biol.* **7**, 581–590 (2005).
32. E. J. Ezratty, C. Bertaux, E. E. Marcantonio, G. G. Gundersen, Clathrin mediates integrin endocytosis for focal adhesion disassembly in migrating cells. *J. Cell Biol.* **187**, 733–747 (2009).
33. G. P. F. Nader, E. J. Ezratty, G. G. Gundersen, FAK, talin and PIPKIγ regulate endocytosed integrin activation to polarize focal adhesion assembly. *Nat. Cell Biol.* **18**, 491–503 (2016).
34. J. A. Broussard, D. J. Webb, I. Kaverina, Asymmetric focal adhesion disassembly in motile cells. *Curr. Opin. Cell Biol.* **20**, 85–90 (2008).
35. E. I. Liang, E. J. Mah, A. F. Yee, M. A. Digman, Correlation of focal adhesion assembly and disassembly with cell migration on nanotopography. *Integr. Biol.* **9**, 145–155 (2017).
36. M. Théry *et al*., Anisotropy of cell adhesive microenvironment governs cell internal organization and orientation of polarity. *Proc. Natl. Acad. Sci. U.S.A.* **103**, 19771–19776 (2006).
37. I. Juhasz *et al*., Growth and invasion of human melanomas in human skin grafted to immunodeficient mice. *Am. J. Pathol.* **143**, 528–537 (1993).
38. X. Sun *et al*., Asymmetric nanotopography biases cytoskeletal dynamics and promotes unidirectional cell guidance. *Proc. Natl. Acad. Sci. U.S.A.* **112**, 12557–12562 (2015).
39. E. D. Tabdanov *et al*., Bimodal sensing of guidance cues in mechanically distinct microenvironments. *Nat. Commun.* **9**, 4891 (2018).
40. R. Zaidel-Bar, C. Ballestrem, Z. Kam, B. Geiger, Early molecular events in the assembly of matrix adhesions at the leading edge of migrating cells. *J. Cell Sci.* **116**, 4605–4613 (2003).
41. A. Boudaoud *et al*., FibrilTool, an ImageJ plug-in to quantify fibrillar structures in raw microscopy images. *Nat. Protoc.* **9**, 457–463 (2014).
42. C. G. Galbraith, K. M. Yamada, M. P. Sheetz, The relationship between force and focal complex development. *J. Cell Biol.* **159**, 695–705 (2002).
43. A. M. Pasapera, I. C. Schneider, E. Rericha, D. D. Schlaepfer, C. M. Waterman, Myosin II activity regulates vinculin recruitment to focal adhesions through FAK-mediated paxillin phosphorylation. *J. Cell Biol.* **188**, 877–890 (2010).
44. P. W. Oakes, Y. Beckham, J. Stricker, M. L. Gardel, Tension is required but not sufficient for focal adhesion maturation without a stress fiber template. *J. Cell Biol.* **196**, 363–374 (2012).
45. J. R. Beach *et al*., Nonmuscle myosin II isoforms coassemble in living cells. *Curr. Biol.* **24**, 1160–1166 (2014).
46. D. T. Burnette *et al*., A contractile and counterbalancing adhesion system controls the 3D shape of crawling cells. *J. Cell Biol.* **205**, 83–96 (2014).
47. A. B. Verkhovsky, T. M. Svitkina, G. G. Borisy, Myosin II filament assemblies in the active lamella of fibroblasts: Their morphogenesis and role in the formation of actin filament bundles. *J. Cell Biol.* **131**, 989–1002 (1995).
48. P. Hotulainen, P. Lappalainen, Stress fibers are generated by two distinct actin assembly mechanisms in motile cells. *J. Cell Biol.* **173**, 383–394 (2006).
49. D. T. Burnette *et al*., A role for actin arcs in the leading-edge advance of migrating cells. *Nat. Cell Biol.* **13**, 371–381 (2011).
50. J. A. Eble, S. Niland, The extracellular matrix in tumor progression and metastasis. *Clin. Exp. Metastasis* **36**, 171–198 (2019).
51. M. W. Conklin *et al*., Aligned collagen is a prognostic signature for survival in human breast carcinoma. *Am. J. Pathol.* **178**, 1221–1232 (2011).
52. C. Leclech, C. Villard, Cellular and subcellular contact guidance on microfabricated substrates. *Front. Bioeng. Biotechnol.* **8**, 551505 (2020).
53. J. Saarikangas, H. Zhao, P. Lappalainen, Regulation of the actin cytoskeleton-plasma membrane interplay by phosphoinositides. *Physiol. Rev.* **90**, 259–289 (2010).
54. V. Swaminathan, G. M. Alushin, C. M. Waterman, Mechanosensation: A catch bond that only hooks one way. *Curr. Biol.* **27**, R1158–R1160 (2017).
55. S. V. Plotnikov, A. M. Pasapera, B. Sabass, C. M. Waterman, Force fluctuations within focal adhesions mediate ECM-rigidity sensing to guide directed cell migration. *Cell* **151**, 1513–1527 (2012).
56. A. M. Pasapera *et al*., Rac1-dependent phosphorylation and focal adhesion recruitment of myosin IIA regulates migration and mechanosensing. *Curr. Biol.* **25**, 175–186 (2015).
57. C. Bonnans, J. Chou, Z. Werb, Remodelling the extracellular matrix in development and disease. *Nat. Rev. Mol. Cell Biol.* **15**, 786–801 (2014).
58. I. Acerbi *et al*., Human breast cancer invasion and aggression correlates with ECM stiffening and immune cell infiltration. *Integr. Biol.* **7**, 1120–1134 (2015).
59. Q. Luo, D. Kuang, B. Zhang, G. Song, Cell stiffness determined by atomic force microscopy and its correlation with cell motility. *Biochim. Biophys. Acta* **1860**, 1953–1960 (2016).
60. V. Swaminathan *et al*., Mechanical stiffness grades metastatic potential in patient tumor cells and in cancer cell lines. *Cancer Res.* **71**, 5075–5080 (2011).
61. S. E. Cross *et al*., AFM-based analysis of human metastatic cancer cells. *Nanotechnology* **19**, 384003 (2008).
62. M. Raudenska *et al*., Cisplatin enhances cell stiffness and decreases invasiveness rate in prostate cancer cells by actin accumulation. *Sci. Rep.* **9**, 1660 (2019).
63. S. Sharma, C. Santiskulvong, J. Rao, J. K. Gimzewski, O. Dorigo, The role of Rho GTPase in cell stiffness and cisplatin resistance in ovarian cancer cells. *Integr. Biol.* **6**, 611–617 (2014).
64. A. Sadok *et al*., Rho kinase inhibitors block melanoma cell migration and inhibit metastasis. *Cancer Res.* **75**, 2272–2284 (2015).
65. R. A. Patel, Y. Liu, B. Wang, R. Li, S. M. Sebti, Identification of novel ROCK inhibitors with anti-migratory and anti-invasive activities. *Oncogene* **33**, 550–555 (2014).
66. E. Sahai, R. Garcia-Medina, J. Pouysségur, E. Vial, Smurf1 regulates tumor cell plasticity and motility through degradation of RhoA leading to localized inhibition of contractility. *J. Cell Biol.* **176**, 35–42 (2007).
67. E. Sahai, C. J. Marshall, Differing modes of tumour cell invasion have distinct requirements for Rho/ROCK signalling and extracellular proteolysis. *Nat. Cell Biol.* **5**, 711–719 (2003).
68. S. Pinner, E. Sahai, Imaging amoeboid cancer cell motility in vivo. *J. Microsc.* **231**, 441–445 (2008).
69. V. Ruprecht *et al*., Cortical contractility triggers a stochastic switch to fast amoeboid cell motility. *Cell* **160**, 673–685 (2015).
70. J. S. Logue *et al*., Erk regulation of actin capping and bundling by Eps8 promotes cortex tension and leader bleb-based migration. *eLife* **4**, e08314 (2015).
71. K. Talkenberger, E. A. Cavalcanti-Adam, A. Voss-Böhme, A. Deutsch, Amoeboid-mesenchymal migration plasticity promotes invasion only in complex heterogeneous microenvironments. *Sci. Rep.* **7**, 9237 (2017).
72. B. S. DeMay, N. Noda, A. S. Gladfelter, R. Oldenbourg, Rapid and quantitative imaging of excitation polarized fluorescence reveals ordered septin dynamics in live yeast. *Biophys. J.* **101**, 985–994 (2011).
73. S. B. Mehta *et al*., Dissection of molecular assembly dynamics by tracking orientation and position of single molecules in live cells. *Proc. Natl. Acad. Sci. U.S.A.* **113**, E6352–E6361 (2016).
74. F. Spira *et al*., Cytokinesis in vertebrate cells initiates by contraction of an equatorial actomyosin network composed of randomly oriented filaments. *eLife* **6**, e30867 (2017).
75. P. O. Strale *et al*., Multiprotein printing by light-induced molecular adsorption. *Adv. Mater.* **28**, 2024–2029 (2016).